Journal of Nuclear Materials 398 (2010) 153–159

Contents lists available at ScienceDirect

Journal of Nuclear Materials

journal homepage: www.elsevier.com/locate/jnucmat

A stability of oxide layers formed in LBE on HCM12A to external loading

Eriko Yamaki [a,*], Kenji Kikuchi [b]

[a] Tokyo Institute of Technology, N1-18, 2-12-1, Ookayama, Meguro-ku, Tokyo 152-8550, Japan
[b] Frontier Research Center for Applied Atomic Sciences, Ibaraki University, Tokai, Ibaraki 319-1106, Japan

A B S T R A C T

Stability of oxide layers associated under applied external load was investigated for oxide layers formed on the inner surface of a steel pipe in flowing LBE with respect to fracture behavior, fracture mechanism and nano-hardness. Ring specimens obtained from the pipe were compressed by a compression test machine, and a fracture of the inner oxide layers was observed. Cracks crossed the oxide layers occurred from the interface between the oxide layers and the base metal to the surface of oxide layers and delamination of oxide layers occurred at the Fe–Cr spinel layer in flatted part of compressed ring specimen. In the compressed part of the ring specimens, all oxide layers were spalled off from the base metal. Engineering strains in the base metal near oxide layers were determined from the deformation of micro-indentation sizes. A tensile strain component to the circumferential direction was responsible for the cracking. It appears that the tensile strain component in the radial direction was responsible for the delamination of the oxide layers. Nano-hardness and Young's modulus of each oxide layers were measured by a nano-indentation method for the evaluation of the fracture behavior. Young's modulus of Fe–Cr spinel layer is lower than that of Fe_3O_4 layer by 10% with the same hardness in both layers, which yields excess strain to the spinel layer rather than to the Fe_3O_4 layer and consequently causes cracking.

1. Introduction

Lead bismuth eutectic (LBE) is expected as a coolant and/or a spallation target in a nuclear energy system including an accelerator driven application. One of the main issues for the application is how to prevent the damage of the structural material steels from the LBE corrosion attacks. The oxide layers, which are formed on the steels by oxygen dissolved in the lead alloy, can be expected to have a protective effect against dissolution of steels. In practical system, thermal stress can be generated on the structural materials by the temperature distribution in a cooling system, a hydrostatic pressure, a nuclear heat generation and a buckling of the structural element [1]. Therefore it is important to investigate how oxide layers behave while their substrate is deformed. Since the protective effect of the oxide layers is expected not only in liquid lead alloys but also in the gas condition, the mechanical properties of the oxide layers formed in air condition have been investigated. The fracture mechanism of oxide layers caused by the external stress and oxide growth stress has been reported by Schütze et al. [2,3]. According these reports, the fracture behavior is dependent on the condition of the oxide layers and the interface between the oxide layer and the base metal. It is expected that the fractures of oxide layers formed in LBE show different behavior from them of the oxide layers formed in the air. In addition, the protective oxide layer formed in LBE was investigated in no-load conditions, or focused on corrosion mechanism and structure of the oxide formation under loading [4], and nano-indentation technique was applied to the oxide layer on ferritic–martensitic steel formed in LBE [5]. However, studies on the stability of oxide layers formed in LBE under external load have not been investigated yet.

In the present study, a compression test technique is adopted on pre-oxidized ring specimens to investigate the stability of oxide layers under applied external load.

2. Experimental methods

2.1. Test specimens

Ring specimens were obtained from a specimen holder channel in the test section of LBE loop at Mitsui Engineering & Ship-building Co., Ltd. [6]. The channel was made of a pipe with outer diameter of 48 mm and wall thickness of 3 mm. The pipe was made from the ferrite/martensite steel HCM12A whose chemical composition is shown in Table 1.

The inner surface of the pipe had been exposed to flowing LBE during the loop operation. Table 2 shows the condition of temperature and oxygen concentration in LBE during the operation. The average velocity of the LBE in the specimen holder channel was 0.5 m/s. The temperature of the LBE was 400–500 °C. The exposure time in total was 5500 h. Oxygen concentration was controlled in the range from 1×10^{-5} to 5×10^{-5} wt.% by adding hydrogen

* Corresponding author.
E-mail address: yamaki.e.aa@m.titech.ac.jp (E. Yamaki).

0022-3115/$ - see front matter Crown Copyright © 2009 Published by Elsevier B.V. All rights reserved.
doi:10.1016/j.jnucmat.2009.10.026

Table 1
Chemical composition of HCM12A (mass%).

Fe	Cr	Si	Mn	Mo	C	Cu	W	Ni	V
Bal.	10.64	0.3	0.61	0.37	0.14	0.84	1.94	0.32	0.19

Table 2
The condition of temperature and oxygen concentration in LBE during the operation.

Time (h)	Temperature (°C)	Oxygen concentration (wt.%)
0–1000	450	5×10^{-6}–5×10^{-5}
1000–2000	500	2×10^{-5}–5×10^{-5}
2000–5000	450	1×10^{-5}–5×10^{-5}
5000–5500	450	5×10^{-6}–5×10^{-5}

and/or moisture with argon carrier gas, and monitored by a Bi/Bi_2O_3 reference type solid electrolyte oxygen sensor.

After the material was exposed to the LBE in the loop, the test section pipe was cut into 6 mm-wide sections (3 rings). One of them was used as a sample for a ring compression test while the one of them was used for nano-indentation measurement. The cross sections of the sample were polished by #2400 paper and then by diamond paste. The cross sections of the sample were characterized using scanning electron microscope (SEM) and energy dispersive X-ray spectroscopy (EDX) before the mechanical testing of the oxide layers.

2.2. Ring compression test

A schematic figure of a compression test is shown in Fig. 1. A ring specimen was fixed between a cross head and a base flat plate of the mechanical test machine. The specimen was compressed to a half of initial diameter, 24 mm, at a constant stroke speed of 5 mm/min.

After the compression test, the cross section and inner surface of ring specimen were investigated by SEM and EDX.

2.3. Measurement of engineering strains

In order to investigate the distribution of the local engineering strains which were introduced into the ring by the compression test, the differences of the size of the indents on the cross section of the ring before and after compression test were measured. Diamond indents were applied on a cross section of the sample before the compression test. Vickers hardness indents (490 N for 15 s) were placed on the sample cross section before the compression testing of the pipe was performed. Indentations were made on the sample cross section as shown in Fig. 2. Each line of indents consists of 10 hardness indents. The size and shape of the indents

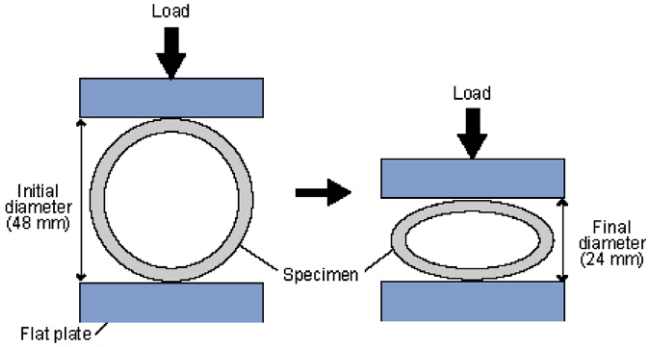

Fig. 1. The schematic figure of the compression test.

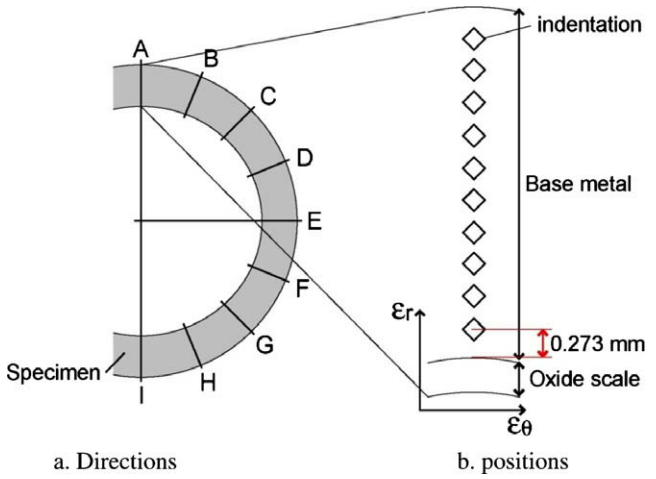

Fig. 2. Directions and positions where indentations were applied on the cross section.

before and after the compression test was measured using an optical microscope. Local engineering strains defined by Eq. (1) were determined from the deference between the initial length of indents before the compression test $L_{initial}$ and the final length of the indents after the compression test L_{final} as shown in Fig. 3.

$$\varepsilon_\theta, \varepsilon_r = \frac{L_{final} - L_{inital}}{L_{initial}} \quad (1)$$

where, ε_θ is the strain to the circumferential direction of the ring, and ε_r is the strain to the radial direction of the ring.

2.4. Nano-indentation

The nano-hardness measurements were preformed with a nano-indentation testing machine (ENT-1100a, ELIONIX INC.) to characterize the mechanical proprieties of the oxide layers and the base metal. A Berkovich diamond indenter was used for nano-indentation test. The indents were applied on the cross section of the samples at a constant loading rate of 4.9 μN/s up to 4.9×10^{-3} N. Each indent was located 5 μm apart from its surrounding indents. The load was kept for 100 s and then released fully at the same constant loading rate. Load–displacement diagrams were recorded for all loading–unloading process. Nano-hardness H, plastic hardness H_P and Young's modulus E were calculated by a standard procedure according to the method of Oliver and Pharr [7] with the results of load–displacement curves shown in Fig. 4. The nano-hardness H was determined from peak load P_{max} and projected area of contact A_S by

$$H = \frac{P_{max}}{A_S} \quad (2)$$

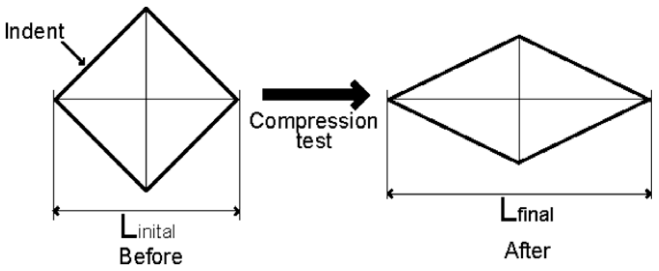

Fig. 3. Measurement method of deference of the indent before and after the compression test.

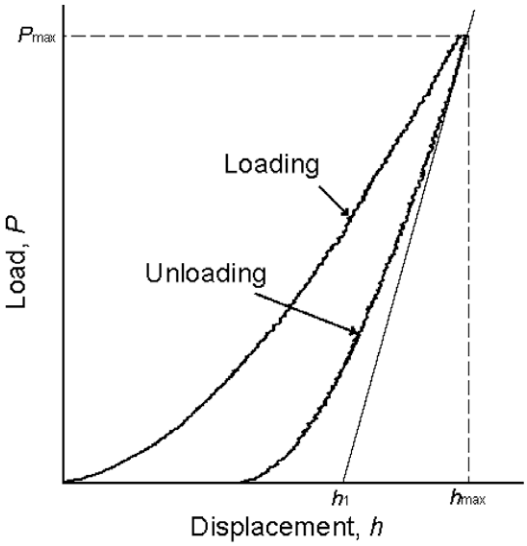

Fig. 4. A schematic presentation of load versus indenter displacement data for an indentation experience.

A_S was given by

$$A_S = \left(3^{3/2}\tan^2\alpha h^2\right)/\sin\alpha = h^2/0.037926 \quad (3)$$

where, α is the face angle from the vertical axis of the indenter (Berkovich indenter: 65°), and h is the displacement. The reduced modulus E^* of the material is obtained by

$$E^* = \frac{\sqrt{\pi}}{2}\frac{S}{\sqrt{A_r}} \quad (4)$$

where, S is the contact stiffness derived from fitting a power law function to the first 50% of the unloading of the load–displacement curve, and A_r is the contact projection area. S = dP/dh is the slope of the load–displacement curve during the unloading cycle. The reduced modulus is a combination of effective contact between an indenter and a test material. The elastic modulus of the tested material can be calculated from

$$\frac{1}{E^*} = \frac{1-v_i^2}{E_i} + \frac{1-v_s^2}{E_S} \quad (5)$$

where, E_S and v_s are Young's elastic modulus and Poisson's ratio of the test material and E_i and v_i are Young's elastic modulus and Poisson's ratio of the indenter. The material parameters E_i = 1050 GPa, v_i = 0.1 and v_S = 0.3 were used.

The plastic hardness H_P was determined by

$$H_P = 0.037926\frac{P_{max}}{h_1^2} \quad (6)$$

where, h_1 is the displacement determined by extrapolation tangential line of the load–displacement curve during the unloading cycle to the horizontal axis in Fig. 4.

The nano-hardness H, the plastic hardness H_P and the Young's modulus E of each layers were compared to each other.

3. Results

3.1. Oxide layer formation

Fig. 5 shows the SEM images and EDX results of the cross section of the ring specimens before compression tests. The average thickness of oxide layers formed on the specimen is about 17 μm. As shown in the EDX results (Fig. 5b) a double oxide layer

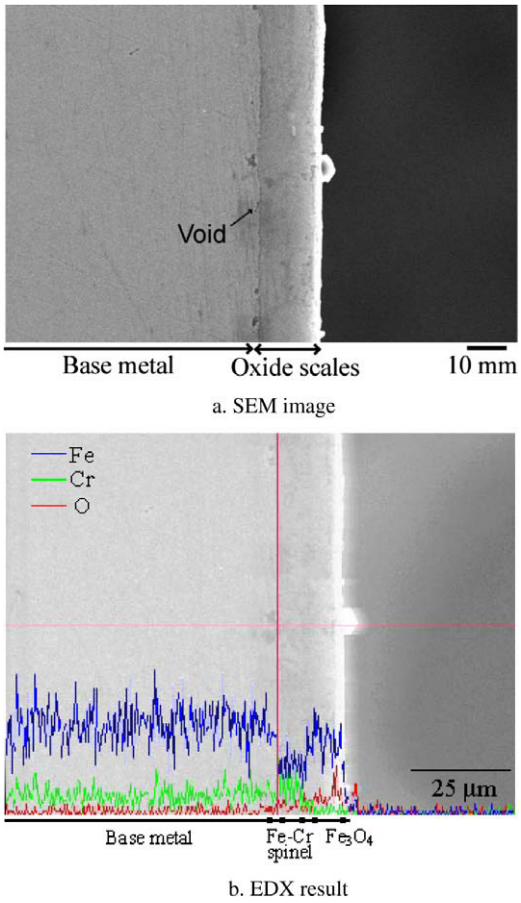

Fig. 5. Cross section of the oxide layers on the inner surface.

was found; the inner layer contained Fe, Cr and O (9 um) and the outer layer contained Fe and O (8 um). According to the literature on oxidation of high chromium martensitic steels in LBE [8–12], this could be the typical magnetite-spinel structure. Therefore, in this article these layers will be addressed like this. The thickness of this layer structure was uniform all over the surface of the sample. Some voids were observed along the interface between Fe–Cr spinel and base metal. It is found that these two oxide layers have no crack and no detachment in the layers with good adhesion along the interfaces between base metal and Fe–Cr spinel and between Fe–Cr spinel and Fe_3O_4.

3.2. Local stain distributions

Fig. 6a shows a specimen after compression. It was compressed to 24 mm during loading and expanded to 27.5 mm after unloading due to an elastic deformation recovery. The ring was flattened in the A–B area and the H–I area, and bent in the C–G area.

Fig. 6b shows a strain distribution at the nearest points to the inner surface, 0.273 mm apart from the interface between the oxide layer and the base metal shown in Fig. 2b. Strain distributions are symmetric along the circumferential position and between radial and circumferential components except for the positions I and E, respectively. The results of strains shows too little value at the position I, and a peak value of 15% at the position E.

3.3. Oxide layers cracking

Fig. 7 shows SEM images of the specimen after compression test. It is found in Fig. 7a that cracks which were across the oxide

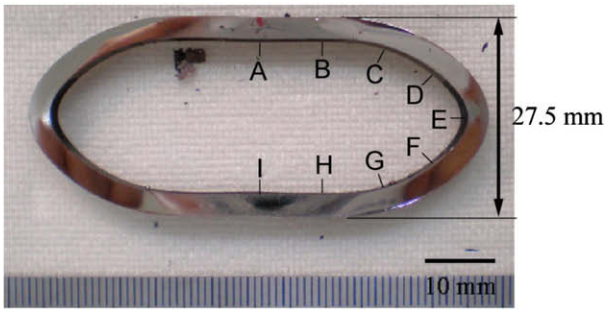

a. The ring compressed 50 %

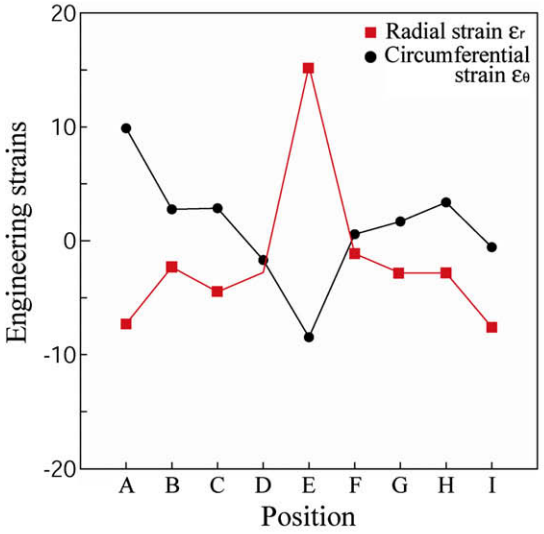

b. Results of engineering strain: The horizontal axis is position of indentations. A-I is same position with Fig. 2a. The vertical axis is engineering strain.

Fig. 6. Rings after large deformation of 50%.

layers from the interface between the oxide layer and the base metal to the surface of oxide layers, and the delamination of oxide layers occurred at the Fe–Cr spinel layer at the position A as shown in Fig. 7a. These cracks and delamination are observed on the whole inner surface the specimen as shown in Fig. 7b. Serveral cracks were found in the oxide layer in Fig. 7b, where some of cracked volume was projected and some of cracked volume was delaminated from the base metal. Intervals between the crack lines are estimated to be a tens μm. Fig. 7c shows the cross section of oxide layers at the B–C area. The cracks crossed the oxide layers from the interface between the oxide layer and the base metal in the same manner as those at the position A. It is recognized that intervals between crack lines were smaller near the position B and larger near the position C, and a fewer delamination damages occurred. There were no cracks and no delaminations in the C–D area as shown in Fig. 7d. Oxide layers were spalled off from the base metal near the position E and remained in the base metal near the position C as shown in Fig. 7e. Fig. 7f shows the cross section of oxide layers at the position E. In this area, all oxide layers were spalled off from the base metal.

3.4. Nano-indentation

Fig. 8 shows the average values of hardness, plastic hardness and Young's modulus of a base metal, Fe_3O_4 layer and Fe–Cr spinel layer. The hardness of the Fe–Cr spinel layer was higher compared to the hardness of the base metal and the magnetite layer. The hardness value is more than twice larger than that of the base metal. The hardness value of Fe_3O_4 is close in value to that of Fe–Cr spinel, although it was lower. Plastic hardness of the oxide layers is about four times larger than that of base metal. The plastic hardness of the Fe–Cr spinel layer was higher compared to the plastic hardness of the base metal and the magnetite layer. The value of Fe–Cr spinel is more than 2 GPa higher than that of Fe_3O_4. Young's modulus of the base metal is the largest among them, while Fe_3O_4 shows larger value than Fe–Cr spinel by 10%.

4. Discussions

Cracks and delaminations in the oxide layers were observed on the specimen deformed by the elastic and plastic deformations during the loading process and the spring-back caused by the removal of the load. However, the specimen passed through a history of loading and the removal of the loading. Fig. 9 shows simulated maximum principal strain distributions of the ring specimen at fully loaded and unloaded conditions calculated by ABAQUS code [13]. The model describes a quarter part of the whole ring structure with having only a base metal property without any consideration on oxide layers. Arrows show induced strain vectors with an optional value. Tensile strains to the circumferential direction were induced in the A–B area and near the position B of the B–C area at fully loaded condition, but disappeared at near the B–C area after the removal of the load due to re-distribution of strains. Tensile strains to the radial direction were induced in the D–E area and near the position E of the C–D area at fully loaded condition, but relaxed in the C–D area after the removal of the load. The shape of the sample after the compression test shows a similar shape with that of loaded one in Fig. 9 possibly because of excessive deformation at the position E in the experiment. Strain distributions obtained from changes of micro Vickers indentation sizes showed too little value at the position I and excessive value at position E as shown in Fig. 6. This might be attributed to the micro-structure property such as grain boundary or local grain deformation. It is concluded that a tensile strain component to the circumferential direction is responsible for the cracking, and a tensile strain component to the radial direction is responsible for the delamination of oxide layers (Fig. 10).

From the image of cross section, the strains in the fractured oxide layers e_{oxi} which is parallel to the circumferential strain were estimated by

$$e_{oxi} = \frac{d_{width}}{d_{interval} + d_{width}} \tag{7}$$

where, d_{width} is the width of cracks crossed the oxide layers and $d_{interval}$ is the interval between cracks. From Fig. 6a and c, the strains in oxide layers at A and B positions e_{oxi} are estimated to be 7% and 5%, respectively. These values are agreeable with measured strains of circumferential components in the base metal 0.273 mm away from the interface between the base metal and the oxide layers as shown in Fig. 6.

The chemical compositions of HCM12A are similar to those of ferritic–martensitic steels, T91 and HT-9. The samples exposed to LBE for more than 5500 h in the LBE loop was used, so that some of oxide layer of Fe_3O_4 might disappear in flowing condition. However, the thickness of Fe–Cr spinel layer and that of Fe_3O_4 are 8 μm and 9 μm, respectively, according to Fig. 5. Hosemann et al. measured the nano-hardness of oxide layers of T91 and HT-9 by means of nano-indentation[5], and reported that the hardness of Fe–Cr spinel and Fe_3O_4 layers on the HT-9 was around 10 GPa, which was nearly equal to the hardness of the oxide layers reported in this study. Young's modulus of the base metal is the largest among

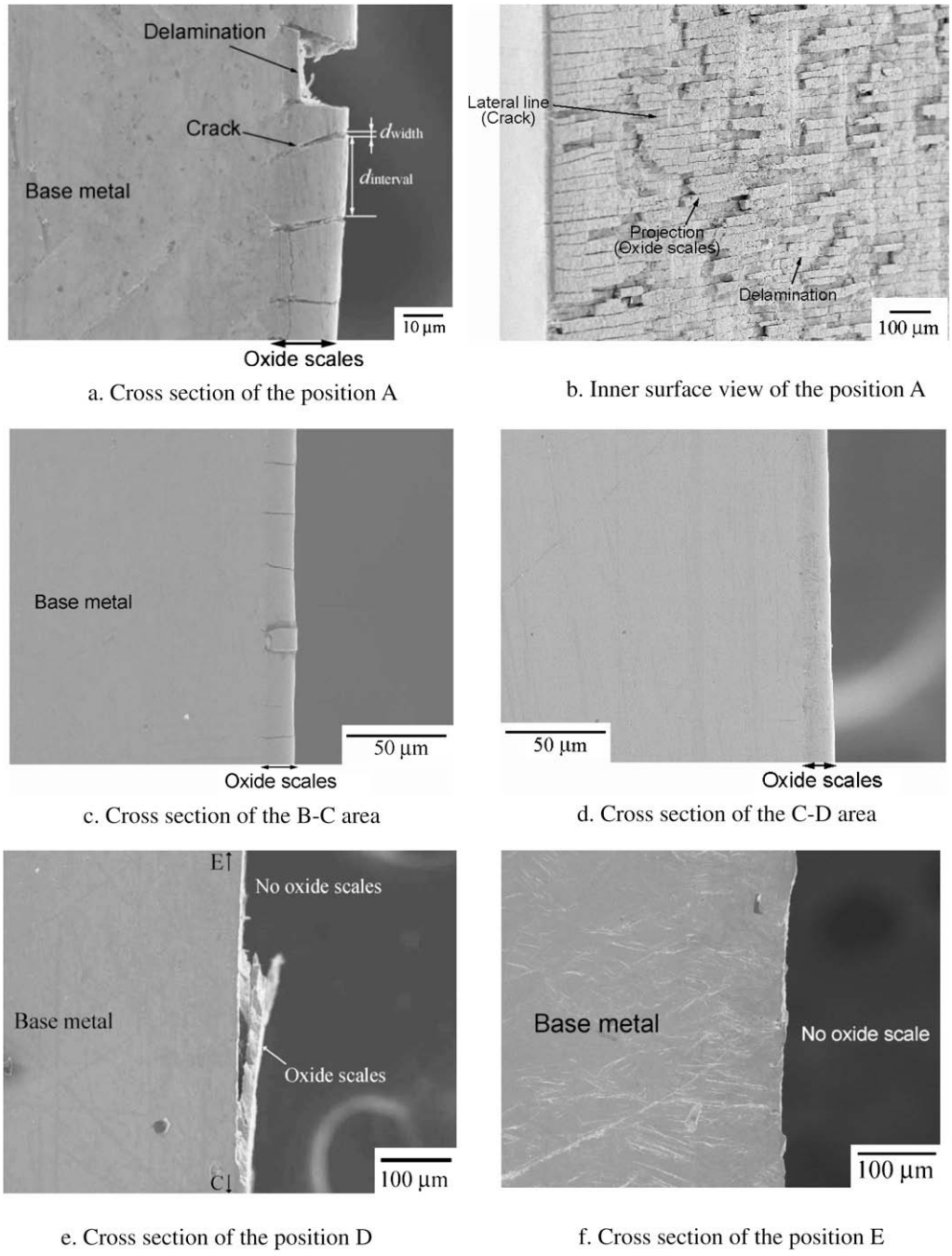

Fig. 7. SEM images of the ring specimen after large deformation compression test.

them, while Fe_3O_4 of 230 GPa is larger than that of Fe–Cr spinel by 10%, which is also similar to HT-9. The mechanical properties measured by nano-indentation of the oxide layers formed on HCM12A in LBE are similar to the measured properties of HT-9 in [5]. According to the reports by Nicholls et al. [14] and by Robertson and Manning [15], the E-modulus of $FeCr_2O_4$ and that of Fe_3O_4 measured of single crystals at room temperature is 233 GPa ($FeCr_2O_4$) and 210 GPa (Fe_3O_4). These values are similar to the results of this study.

The strain introduced to the circumferential direction in the oxide layers caused three types of brittle fracture behaviors of the oxide layers: cracks crossed the oxide layers, delamination parallel to the interface between the oxide layer and the base metal and spall off of the oxide layers. It is speculated that cracks crossed the oxide layers appeared first, where the number of the cracks increases with increasing of the circumferential strain; then delamination appeared at the interface between the oxide layer and the base metal and/or in a plane of Fe–Cr spinel layer; and finally with increasing of the strain, the oxide layers spall off. This compression test allows observing that there are two kinds of critical strains at the same time: one of them was the critical strain for cracking crossed the oxide layers, $\varepsilon_{C,1}$, another was that for the delamination, $\varepsilon_{C,2}$. The $\varepsilon_{C,1}$ is generally given by the Eq. (8) [2,3],

$$\varepsilon_{C,1} = \frac{K_{Ic}}{fE_{oxide}\sqrt{\pi c}} \tag{8}$$

where, K_{Ic} is the fracture toughness of the oxide sales, f is geometrical values of a surface notch of infinite length, c is half the length

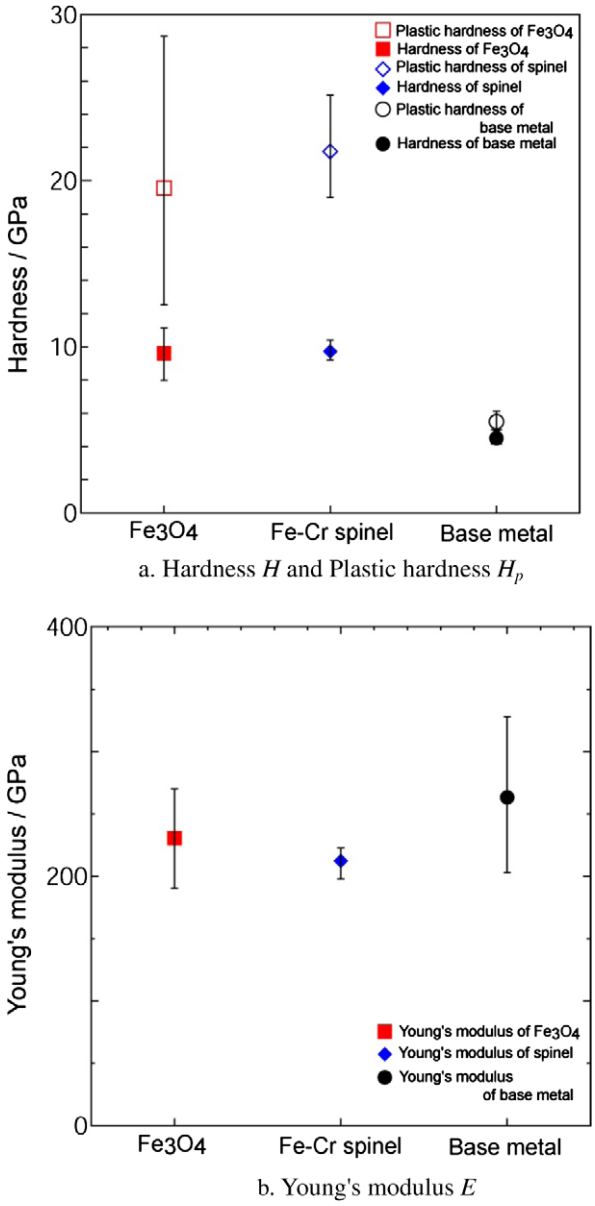

Fig. 8. The average values of hardness, plastic hardness and Young's modulus of a base metal, Fe_3O_4 layer and Fe–Cr spinel layer measured by nano-indentation method. The vertical lines on the each point show the range of the each values which were by 20 indents on Fe_3O_4, 13 indents on Fe–Cr spinel and 10 indents on the base metal.

of an embedded defect or the whole length of a surface defect. K_{Ic} can be calculated from surface fracture energy values of the oxide by

$$K_{Ic} = \sqrt{2\gamma_0 E_{oxide}} \tag{9}$$

Because the E-modulus of Fe–Cr spinel is larger than that of Fe_3O_4 according to the results of nano-indentation measurement, $\varepsilon_{C,1}$ of Fe–Cr spinel is smaller than Fe_3O_4. This may be one of the reasons why cracking crossed the oxide layer started in Fe–Cr spinel layer. The $\varepsilon_{C,2}$ can be described by

$$\varepsilon_{C,2} = \frac{K_{Ic}}{f\sqrt{\pi c}} \cdot \frac{(1 + r/d)(1 + \nu)}{2E_{oxide}} \tag{10}$$

Because $\varepsilon_{C,2}$ of Fe–Cr spinel is smaller than Fe_3O_4, it can be considered that this is one of the reasons why the delamination cracking occurs in Fe–Cr spinel layer. However, it is found that there are

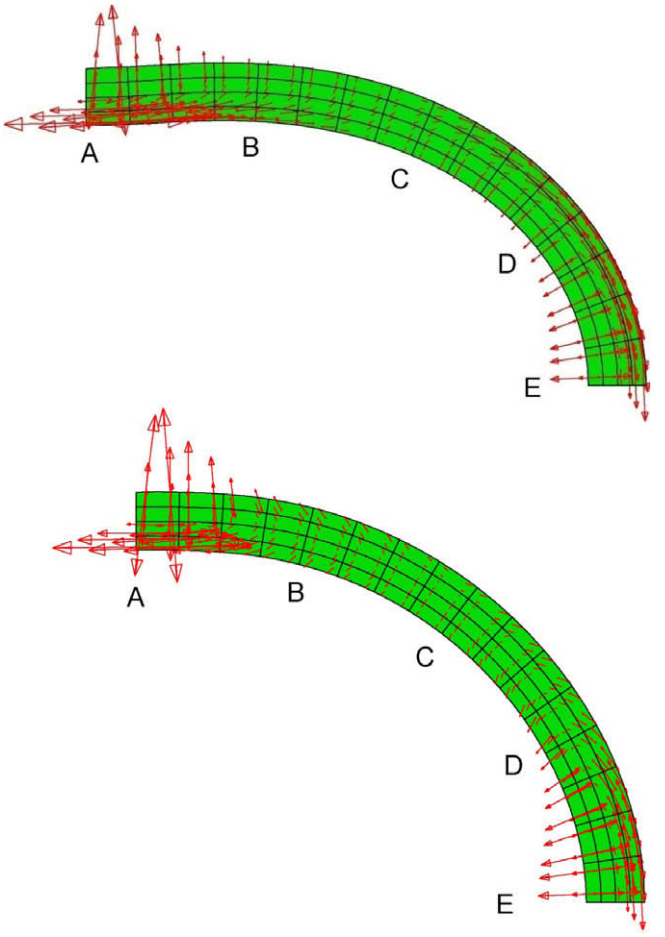

Fig. 9. Simulation of maximum principal strain distribution induced at loading (top) and unloading (bottom) conditions.

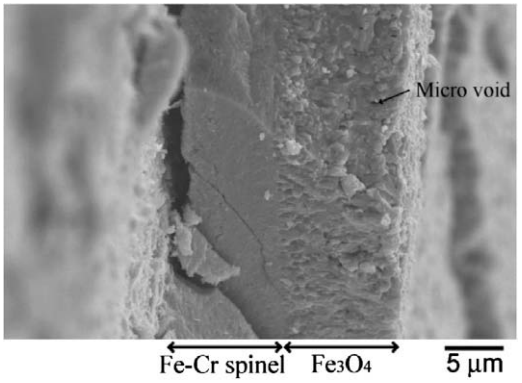

Fig. 10. Detailed SEM observation of fractured oxide layers of Fig. 7b.

voids along the interface between Fe–Cr spinel and base metal. These voids cause the adhesion of the oxide layers decreasing. This fact may be also one of the reasons for the occurrence of the delamination.

5. Conclusion

A compression test was performed to investigate the fracture behavior of the oxide layers formed in LBE under several strain levels, and nano-indentation measurement was performed to

measure the mechanical properties of oxide layers and the base metal (HCM12A). The conclusion could be obtained as follows:

In the flattened area of the compressed specimen, the cracks across oxide layers occurred from the interface between the oxide layer and the base metal to the surface of oxide layers, and the delamination of oxide layers occurred at the Fe–Cr spinel layer. In the bent area of the compressed ring specimen, all oxide layers spalled off from the base metal. According to the local deformations obtained from measured engineering strains of the base metal and calculated maximum principal strain distributions of the ring specimen, a tensile strain component to the circumferential direction was responsible for the cracking, and a tensile strain component to the radial direction was responsible for the delamination of oxide layers.

Cracking occurred due to an excess strain to the spinel layer rather than Fe_3O_4 layer that was caused by the fact that the Young's modulus of Fe–Cr spinel layer was lower than that of Fe_3O_4 layer by 10% with the same hardness in both layers.

Acknowledgement

The specimen supply by the Mitsui Engineering and Ship-building Co., Ltd. is highly acknowledged. The nano-indentation measurement was supported by Yuichiro Ono (Graduate School of Science and Engineering, Tokyo Institute of Technology). The authors would like to thank Associate Professor Minoru Takahashi of Tokyo Institute of Technology for many constructive suggestions and supports.

Reference

[1] W. Ma, E. Bubelis, A. Karbojian, B.R. Sehgal, P. Coddington, Nuclear Engineering and Design 236 (2006) 1422.
[2] M. Schütze, Oxidation of Metals 44 (1995) 29.
[3] M. Schütze, S. Ito, W. Przybilla, H. Echsler, C. Bruns, High-Temperature Corrosion and Protection (2000) 19.
[4] H. Glasbrenner, F. Groschel, Journal of Nuclear Materials 356 (2006) 213.
[5] P. Hosemann, J.G. Swadener, J. Welch, N. Li, Journal of Nuclear Materials 377 (2008) 201.
[6] K. Kikuchi, K. Kamata, M. Ono, T. Kitano, K. Hayashi, H. Oigawa, Journal of Nuclear Materials 377 (2008) 232.
[7] W.C. Oliver, G.M. Pharr, Journal of Material Research 7 (1992) 1564.
[8] D.G. Briceno, L.S. Crespo, F.J. Martin Munoz, F.H. Arroyo, Journal of Nuclear Materials 303 (2002) 137.
[9] C. Fazio, G. Benamati, C. Martini, G. Palombarini, Journal of Nuclear Materials 296 (2001) 243.
[10] T. Furukawa, G. Müller, G. Schumacher, A. Weisenburger, A. Heinzel, F. Zimmermann, K. Aoto, Journal of Nuclear Science and Technology 41 (2004) 265.
[11] G. Müller, A. Heinzel, J. Konys, G. Schumacher, A. Weisenburger, F. Zimmermann, V. Engelko, A. Rusanov, V. Markov, Journal of Nuclear Materials 335 (2004) 163.
[12] F. Barbier, G. Benamati, C. Fazio, A. Rusanov, Journal of Nuclear Materials 295 (2001) 149.
[13] ABAQUS/Standard, V6.7, SIMULIA.
[14] J.R. Nicholls, D.J. Hall, P.F. Tortorelli, Material at High Temperature 12 (1994) 141.
[15] J. Robertson, M.I. Manning, Material Science and Technology 6 (1990) 81.